

Unveiling the Antibacterial Mechanism of Gold Nanoclusters via In Situ Transmission Electron Microscopy

Jui-Chi Kuo,[○] Shih-Hua Tan,[○] Yu-Cheng Hsiao,[○] Chinmaya Mutalik, Hui-Min Chen, Sibidou Yougbaré, and Tsung-Rong Kuo*



Cite This: *ACS Sustainable Chem. Eng.* 2022, 10, 464–471



Read Online

ACCESS |



Metrics & More



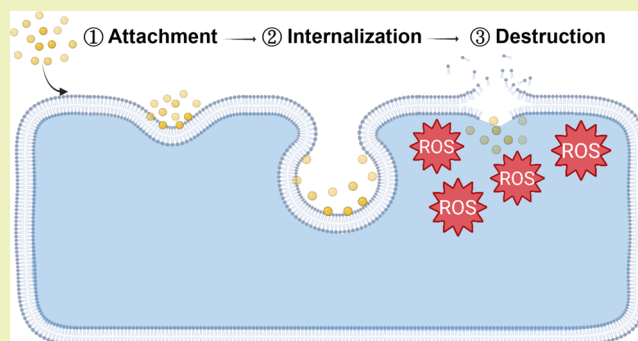
Article Recommendations



Supporting Information

ABSTRACT: Metal nanoclusters (NCs) with unique chemical and physical properties have been extensively demonstrated to be emerging nanoantibiotics for fighting bacterial infections. Understanding the antibacterial mechanisms of metal nanoclusters is important for evaluating their clinical applications as nanoantibiotics. To understand the antibacterial mechanism, gold nanoclusters (AuNCs) were applied as an antibacterial agent for real-time observations of their interactions with bacteria by in situ transmission electron microscopy (TEM). In this work, a surface ligand of glutathione-conjugated (GSH)-AuNCs was prepared via a simple hydrothermal method. Optical and structural characterizations validated the successful preparation of GSH-AuNCs. Bacterial growth curves of *Acetobacter aceti* revealed that the antibacterial activity of GSH-AuNCs increased with the weight concentration. The antibacterial activity of GSH-AuNCs was confirmed by the intracellular reactive oxygen species (ROS) generation induced by GSH-AuNCs in *A. aceti*. Furthermore, real-time observations of interactions between GSH-AuNCs and *A. aceti* were made using in situ liquid cell TEM. Based on the results of real-time observations, GSH-AuNCs first attached onto the bacterial membranes of *A. aceti* by physical adsorption and then penetrated into *A. aceti* by internalization. Eventually, the production of intracellular ROS induced by GSH-AuNCs caused destruction of the bacterial membranes, which led to the death of *A. aceti*. After the bacterial membranes had been destroyed, *A. aceti* eventually died.

KEYWORDS: nanocluster, in situ TEM, antibacterial mechanism, real-time observation, reactive oxygen species



INTRODUCTION

Metal nanoclusters (NCs) composed of several up to a hundred metal atoms have revealed superior structural and optical properties, such as facile surface modification, tunable fluorescence, large Stokes shifts, and excellent photostability.^{1–8} After functionalization with various surface ligands, metal NCs have been intensively explored for applications in the fields of energy conversion, biomedical engineering, and nanomedicine.^{9–21} For example, metallic molybdenum NCs were used in a semiliquid cathode assembled with a lithium polysulfide solution, carbon nanofibers, and carbon nanotubes to enable rapid catalytic conversion of the lithium polysulfide solution and ordinary deposition of lithium sulfide.²² Gold NCs (AuNCs) protected by a glutathione (GSH) surface ligand were introduced as a light absorber to facilitate the slow kinetics of electron transfer in a photosynthetic biohybrid system.²³ Cysteine-modified AuNCs were designed as fluorescent probes to evaluate their metabolic mechanism in *Escherichia coli*.²⁴ Fluorescent AuNCs modified with glucose were prepared as a probe to target the overexpression of glucose transporters in brain cancer cells.²⁵ Among various types of metallic NCs, AuNCs revealed the greatest potential

for diverse applications due to their easy preparation, well-defined structure, and stability in water.

Recently, AuNCs have been extensively demonstrated as nanoantibiotics for treating bacterial infections because of their unique chemical and physical properties.^{26–30} Significant achievements have been made in the design of AuNCs with different functional ligands such as amino acids, peptides, enzymes, and antibiotics for antibacterial applications.^{31–36} For instance, peptide-conjugated AuNCs loaded with vancomycin showed higher antimicrobial activity compared to vancomycin alone against both Gram-positive *Staphylococcus aureus* and Gram-negative *E. coli*.³⁷ AuNCs decorated with glutathione and a positive quaternary ammonium ligand were fabricated as an antibacterial agent against multidrug-resistant Gram-positive bacteria.³⁸ AuNCs composed of 25 gold atoms and

Received: October 4, 2021

Revised: December 10, 2021

Published: December 28, 2021



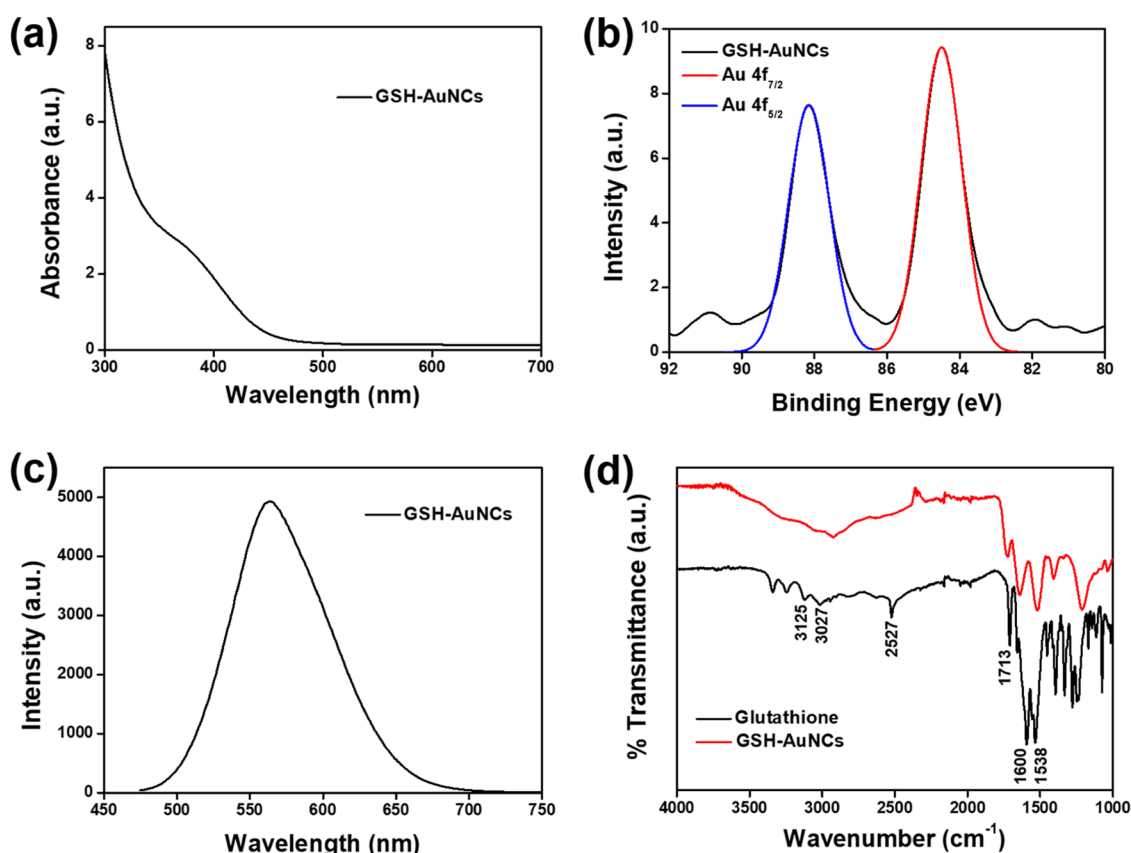


Figure 1. (a) UV-vis absorption spectrum of glutathione-conjugated gold nanoclusters (GSH-AuNCs). (b) XPS spectra of GSH-AuNCs (black line), simulated peak of Au 4f_{7/2} (red line), and simulated peak of Au 4f_{5/2} (blue line). (c) Fluorescence spectrum of GSH-AuNCs. (d) FTIR spectra of glutathione (black) and GSH-AuNCs (red).

18 thiolate ligands of 6-mercaptohexanoic acid exhibited remarkable antibacterial efficiency in killing Gram-negative bacteria.³⁹ Moreover, AuNCs protected by the 6-mercaptohexanoic acid ligand proved to have antibacterial activity for both Gram-negative and Gram-positive bacteria because the ultra-small AuNCs could penetrate into bacteria to induce the generation of intracellular reactive oxygen species (ROS).⁴⁰ Although these great advancements have demonstrated promising applications of AuNCs as wide-spectrum antibacterial agents, in situ observations of the antibacterial mechanisms of AuNCs are still lacking.

In situ techniques such as X-ray absorption spectroscopy, X-ray diffraction, Raman spectroscopy, scanning electron microscopy (SEM), and transmission electron microscopy (TEM) have been widely utilized to provide fundamental information about catalytic systems, material reactions, and real-time imaging.^{41–45} Based on in situ X-ray absorption spectroscopy, the interface between metallic nickel and semiconducting porous silicon wire was verified to generate a photoinduced adaptive structure for oxygen evolution under light irradiation.⁴⁶ With the use of in situ X-ray absorption spectroscopic, Raman spectroscopic, and TEM examinations were carried out, which reveal the real-time structure of CoSe₂ electrocatalysts during both hydrogen and oxygen evolution reactions.⁴⁷ In aluminum ion batteries, real-time monitoring of AlCl₄⁻ intercalated into a flexuous graphite cathode was confirmed using in situ SEM and X-ray diffraction.⁴⁸ In situ TEM was performed to locally heat silver nanoparticles (NPs) by an electron beam, and sublimation of silver NPs was simultaneously observed by in situ TEM.⁴⁹ These advanced in

situ techniques have shown great advantages in measuring catalytic systems down to the single-molecule level and material formation and transformation at the nanoscale level.

Investigating antibacterial mechanisms is an important task for evaluating nanoantibiotics in clinical applications. In this work, to observe the antibacterial mechanism of AuNCs in bacteria, AuNCs conjugated with a surface ligand of glutathione (GSH-AuNCs) were first prepared by a simple hydrothermal method. Optical and structural examinations of GSH-AuNCs were carried out using ultraviolet–visible (UV-vis) spectroscopy, X-ray photoelectron spectroscopy (XPS), fluorescence spectroscopy, Fourier-transform infrared (FTIR) spectroscopy, TEM, and energy-dispersive X-ray (EDX) spectroscopy. Moreover, bacterial growth curves of *A. aceti* incubated with different weight concentrations of GSH-AuNCs were investigated. To examine the antibacterial activity, ROS generation of *A. aceti* incubated with GSH-AuNCs was measured. Most importantly, real-time observations of interactions between GSH-AuNCs and *A. aceti* were confirmed by in situ liquid cell TEM.

EXPERIMENTAL SECTION

Synthesis of GSH-AuNCs. GSH-AuNCs were prepared via a simple hydrothermal method.³² To prepare GSH-AuNCs, 25 mL of an L-glutathione aqueous solution (25 mM) was poured into 25 mL of a chloroauric acid aqueous solution (1 wt %) in a water bath at 40 °C under stirring at 200 rpm. The color of the reaction solution changed from transparent to dark brown, and finally to transparent. Afterward, the reaction solution was stirred at 40 °C and 200 rpm in the dark for 5 days. After reacting for 5 days, to purify the solution, it was

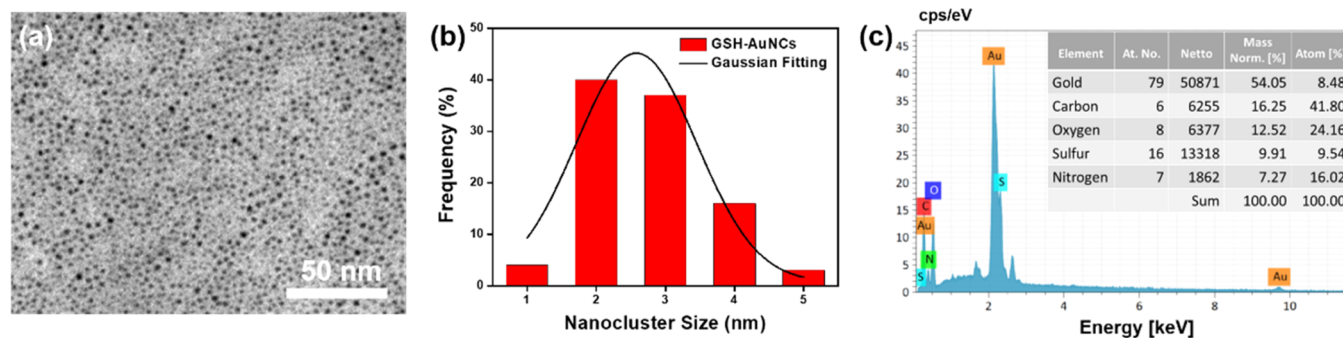


Figure 2. (a) TEM image of glutathione-conjugated gold nanoclusters (GSH-AuNCs). (b) Histogram of the size distribution of GSH-AuNCs and the Gaussian fitting curve. (c) EDX analysis of GSH-AuNCs.

centrifuged at 15 000 rpm for 5 min. The supernatant was removed, and ethanol was added to form a yellow cloudy mixture at the bottom of the centrifuge tube. The solution with the yellow cloudy mixture was precipitated by centrifugation at 18 000 rpm for 10 min. After removal of the supernatant, the precipitate of GSH-AuNCs was dispersed in deionized water by sonication and stored at 4 °C in a dark environment for subsequent experiments.

Antibacterial Activity Test of GSH-AuNCs. Acetic acid bacterium *A. aceti* was utilized to investigate the antibacterial activity of GSH-AuNCs. To culture *A. aceti*, the medium was prepared by adding 5 g of yeast extract, 3 g of peptone, and 25 g of mannitol to 1 L of deionized water. Afterward, the culture medium was sterilized at 121 °C for 15 min. The cryopreserved stock of *A. aceti* was thawed and cultured in 3 mL of the culture medium, and then incubated in a shaker at 170 rpm and 26 °C for the following antibacterial test. To examine the antibacterial activity, an *A. aceti* solution (1.5 mL) was incubated with 1.5 mL of solutions containing various concentrations of 0.125, 0.25, 0.5, and 1.0 mg/mL GSH-AuNCs. The *A. aceti* solutions incubated with GSH-AuNCs were cultured on a shaker at 170 rpm and 26 °C, and their optical density values at a wavelength of 600 nm (OD600) were measured every 30 min. Bacterial growth curves of *A. aceti* incubated with different concentrations of GSH-AuNCs were used to evaluate the antibacterial activities.

Measurement of Intracellular ROS Production. To measure ROS production, the 2',7'-dichlorodihydrofluorescein diacetate (DCFDA) dye was utilized to evaluate intracellular ROS concentrations. In the presence of ROS, DCFDA is rapidly deacetylated and oxidized to 2',7'-dichlorofluorescein (DCF). The fluorescence intensity of DCF (excitation/emission at 488/525 nm) was used to calculate the total amount of ROS produced. Moreover, fluorescent Hoechst 33342 dye (excitation/emission at 350/461 nm) was employed to assess the total amount of *A. aceti*. In this work, the solutions of *A. aceti* (1.5 mL, OD600 = 0.3) were respectively incubated with 1.5 mL of GSH-AuNC solutions (0.125, 0.25, 0.5, and 1 mg/mL) at 170 rpm and 26 °C for 240 min. Afterward, 0.6 μL of Hoechst 33342 and 0.6 μL of DCFDA were added to 600 μL of *A. aceti* incubated with the GSH-AuNC solutions, and the mixtures were incubated at 170 rpm and 26 °C for 30 min in the dark. After incubating for 30 min, the *A. aceti* solutions with GSH-AuNCs, Hoechst 33342, and DCFDA were precipitated by centrifugation at 10 000 rpm for 2 min. The supernatants were discarded, and the pellets were dissolved in 600 μL of sterilized water by vortexing. The fluorescence intensities of DCF and Hoechst 33342 were detected using a microplate reader. ROS production was calibrated to the total number of *A. aceti*. The relative ROS level from the experiment was systematically evaluated and compared to the ROS level of the control. For the control experiment, the ROS level of *A. aceti* incubated in sterilized water was set to 1.0. To eliminate the interference of DCF fluorescence, the fluorescence intensities of 1.5 mL of GSH-AuNC solutions (0.125, 0.25, 0.5, and 1 mg/mL) incubated with the culture medium of *A. aceti* were, respectively, applied as blanks. The blanks of the GSH-AuNC solutions (0.125, 0.25, 0.5, and 1 mg/mL) were separately subtracted from the

fluorescence intensities of DCF from *A. aceti* solutions incubated with the GSH-AuNC solutions (0.125, 0.25, 0.5, and 1 mg/mL).

Sample Preparation for In Situ TEM. To prepare a sample for in situ liquid cell TEM, 1 mL of the *A. aceti* solution (OD600 = 0.5) was first incubated with 1 mL of a GSH-AuNC (1.0 mg/mL) solution. Afterward, 2 μL of the solution containing *A. aceti* and GSH-AuNCs was loaded into the K-kit (Materials Analysis Technology, MA-Tek) through capillary force. After filling with the *A. aceti* and GSH-AuNC solution, the channel openings at both ends of the K-kit were covered with Torr Seal epoxy resin. A copper grid was placed over the K-kit to prepare it for in situ TEM.

RESULTS AND DISCUSSION

Optical and Structural Properties of GSH-AuNCs.

Optical properties of GSH-AuNCs were first characterized by UV-vis spectroscopy. In Figure 1a, the absorption of GSH-AuNCs exhibited a distinct absorption peak at ~380 nm due to the transition between the highest occupied molecular orbital and the lowest unoccupied molecular orbital.⁵⁰ Furthermore, the absorption of GSH-AuNCs revealed no plasmonic absorption from the gold NPs at 520 nm.⁵¹ The vanishing plasmonic absorption of GSH-AuNCs could be attributed to the gold cores of GSH-AuNCs revealing high oxidation states, leading to a shortage of free electrons to induce coherent oscillations.⁵² Moreover, XPS spectra were utilized to examine the oxidation states of the gold cores of the GSH-AuNCs. As shown in Figure 1b, the XPS spectrum of GSH-AuNCs displayed binding energies of Au 4f_{5/2} and Au 4f_{7/2} which, respectively, appeared at 88.2 and 84.5 eV. The simulated binding energies of Au 4f_{5/2} and Au 4f_{7/2} also, respectively, appeared at 88.2 and 84.5 eV. For bulk gold, the binding energies of Au 4f_{5/2} and Au 4f_{7/2}, respectively, appeared at 87.4 and 84.0 eV. Compared to bulk gold, increases in the binding energies of Au 4f_{5/2} and Au 4f_{7/2} of the GSH-AuNCs demonstrated that the gold cores of GSH-AuNCs possessed high oxidation states consistent with the absorption properties of the GSH-AuNCs. The optical fluorescence of the GSH-AuNCs was further characterized at an excitation wavelength at 410 nm. In the fluorescence spectrum of Figure 1c, the GSH-AuNCs displayed a maximum fluorescence intensity at a wavelength of 563 nm, corresponding to the fluorescent mechanism of aggregation-induced emission (AIE). Previous studies have demonstrated that the AIE fluorescence of GSH-AuNCs is caused by the aggregation of Au(I)-GSH motifs on the surface of NCs.^{53–58} Furthermore, to verify the formation of Au–S bonds, FTIR spectra were applied to characterize glutathione before and after modification with AuNCs. As shown in Figure 1d, the FTIR spectrum of glutathione (black curve) revealed characteristic absorption peaks at 2527 (S–H

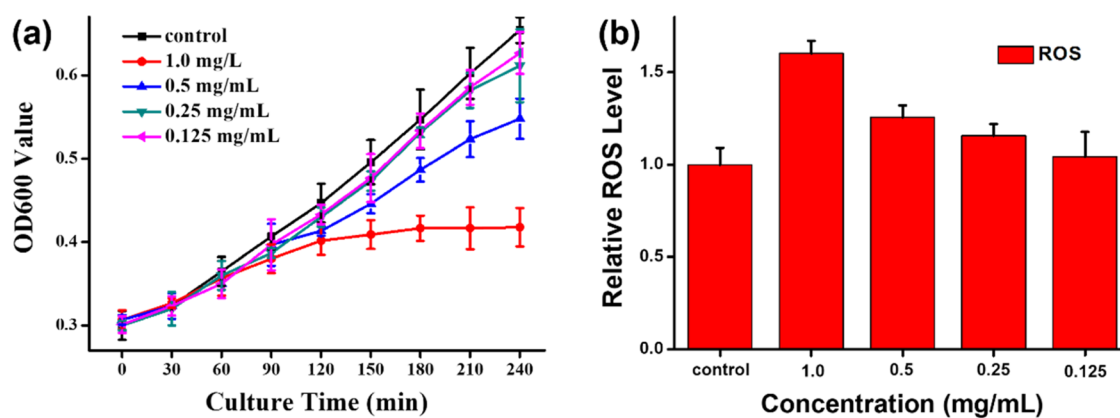


Figure 3. (a) Growth curves of *Acetobacter acetii* incubated with various concentrations (0.125, 0.25, 0.5, and 1.0 mg/mL) of glutathione-conjugated gold nanoclusters (GSH-AuNCs). In the growth curve of the control experiment, *A. acetii* was incubated in sterilized water. (b) In the control experiment, the ROS level of *A. acetii* incubated in sterilized water was set to 1.0. After *A. acetii* was incubated with GSH-AuNCs (0.125, 0.25, 0.5 and 1.0 mg/mL) for 240 min, intracellular ROS production was measured. All data are presented as the mean \pm standard deviation, $n = 3$ per group.

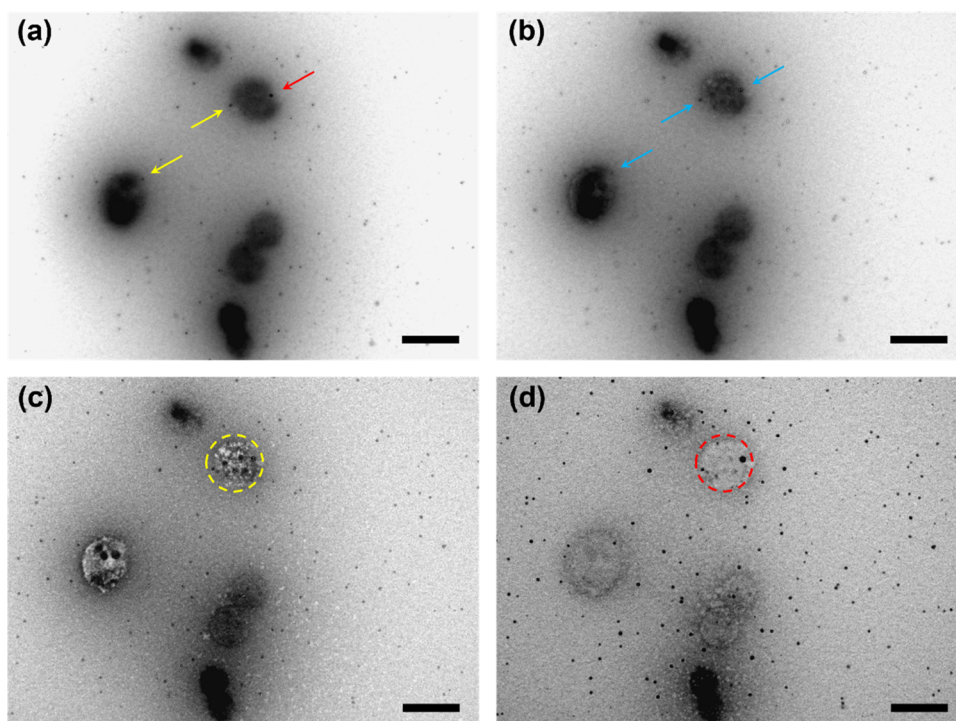


Figure 4. In situ TEM images of (a) attachment and internalization, (b) destruction in the early stage, (c) significant destruction, and (d) complete destruction of glutathione-conjugated gold nanocluster (GSH-AuNC)-treated *A. acetii*. The time for observation of (a) 80, (b) 86, (c) 96, and (d) 114 min after GSH-AuNCs were incubated with *A. acetii*. Yellow arrow: GSH-AuNCs attached onto the bacterial membrane. Red arrow: GSH-AuNCs penetrated into *A. acetii*. Blue arrow: GSH-AuNCs were located around the bacterial membrane. Yellow circle: bacteria revealed collapse. Red circle: bacteria exhibited complete destruction. The scale bar is 2 μm .

stretching bands), 3125 and 3207 (N–H stretching bands), 1600 and 1713 (C=O stretching bands), and 1538 cm^{-1} (N–H deformation of amide bonds).⁵⁹ After the formation of GSH-AuNCs, the FTIR spectrum of glutathione on the GSH-AuNCs exhibited a slight shift and relative broadening compared to that of pure glutathione due to a change in the dipole moment of glutathione.⁶⁰ Most importantly, S–H stretching bands of glutathione disappeared from the FTIR spectrum of GSH-AuNCs. The disappearance of the S–H stretching bands of GSH-AuNCs can be attributed to the formation of Au–S covalent bonds between glutathione and AuNCs.⁶¹

To characterize the size and shape, GSH-AuNCs were examined by TEM. As shown in Figure 2a, GSH-AuNCs were homogeneously distributed on the copper grid due to the conjugation of glutathione onto the surface of AuNCs which prevented aggregation. GSH-AuNCs presented an approximately round shape. The size distributions GSH-AuNCs were measured as shown in the histogram of Figure 2b based on 100 NCs in the TEM image of Figure 2a. According to the histogram of Figure 2b, the simulated Gaussian fitting curve is illustrated in Figure 2b. The average size of GSH-AuNCs was calculated to be 2.6 ± 0.18 nm via the Gaussian fitting curve. Moreover, in Figure 2c, the EDX analysis of GSH-AuNCs

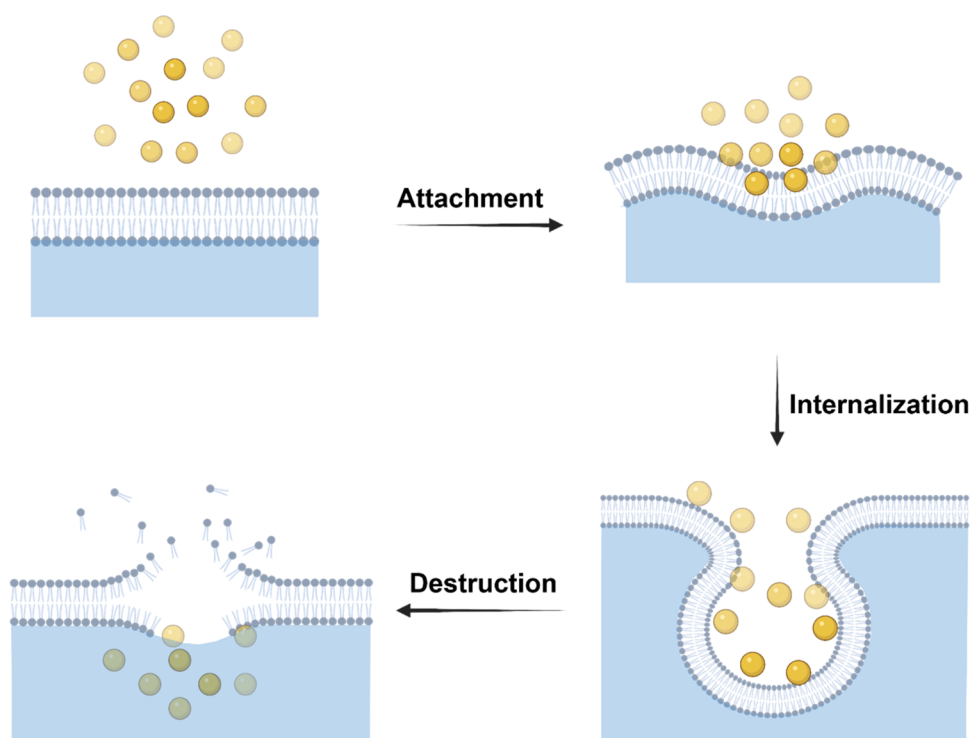


Figure 5. Illustration of the mechanism of the glutathione-conjugated gold nanocluster (GSH-AuNC)-induced death of *A. acetii*.

revealed that they were composed of gold (54.05 wt %), carbon (16.25 wt %), oxygen (12.52 wt %), sulfur (9.91 wt %), and nitrogen (7.27 wt %). EDX analysis demonstrated that GSH-AuNCs were composed of gold and glutathione. Overall, the optical and structural characterizations including the UV–vis absorption spectrum, XPS spectra, fluorescence spectra, FTIR spectra, TEM images, and EDX analysis results demonstrated the successful synthesis of GSH-AuNCs by a facile hydrothermal approach.

Antibacterial Activity of GSH-AuNCs. To investigate the antibacterial activity, various concentrations of GSH-AuNCs were incubated with *A. acetii*. As shown in the bacterial growth curves of Figure 3a, in the control experiment, the OD600 value of the *A. acetii* solution was ~ 0.66 after culturing for 240 min. Furthermore, the OD600 values of *A. acetii* solutions incubated with different GSH-AuNC concentrations of 0.125, 0.25, 0.5, and 1.0 mg/mL were 0.63, 0.61, 0.55, and 0.42, respectively, after culturing for 240 min. The results of the bacterial growth curves indicated that the antibacterial activity increased with the concentration of GSH-AuNCs. Several studies demonstrated that AuNCs exhibit superior antibacterial activity due to their ability to induce intracellular ROS generation in bacteria. To further evaluate ROS generation in bacteria, an H_2DCFDA assay was applied to measure intracellular ROS production after *A. acetii* was incubated with GSH-AuNCs. After incubation of *A. acetii* and GSH-AuNCs for 240 min, the relative ROS levels at various GSH-AuNC concentrations of 0.125, 0.25, 0.5, and 1.0 mg/mL were, respectively, 1.04-, 1.16-, 1.26-, and 1.6-fold, as shown in Figure 3b. Although the surface ligand of GSH is a ROS quencher (Figure S1), intracellular ROS production was still augmented with an increase in the concentration of GSH-AuNCs. Overall, the main reason for the death of *A. acetii* was attributed to the increased intracellular ROS generation after incubation with GSH-AuNCs

Real-Time Observation of Interactions between GSH-AuNCs and *A. acetii*. Recently, antimicrobial processes of AuNCs have been observed under a confocal microscope using their intrinsic fluorescence.^{62,63} To further study the interaction mechanism between GSH-AuNCs and Gram-negative *A. acetii*, alternative real-time observations were conducted by in situ liquid cell TEM. In the control experiment without GSH-AuNC incubation, there was no significant change in *A. acetii*, as shown in Supporting Information Figure S2 and Video S1 (play at 16-speed). Moreover, real-time TEM images of *A. acetii* incubated with GSH-AuNCs were acquired as shown in Figure 4. In Figure 4a, GSH-AuNCs first attached to the bacterial membrane as indicated by the yellow arrow. Afterward, GSH-AuNCs penetrated into *A. acetii* by bacterial internalization as indicated by the red arrow. At this stage, GSH-AuNCs also induced destruction of the bacterial membrane. In Figure 4b, after bacterial internalization, GSH-AuNCs were located around the bacterial membrane as indicated by the blue arrow, and this led to damage of *A. acetii*. As shown in Figure 4c, the bacteria revealed obvious collapse as indicated by the yellow circle. In Figure 4d, in the end, the bacteria exhibited complete destruction as indicated by the red circle. The real-time TEM video for the interaction between GSH-AuNCs and *A. acetii* is provided in Supporting Information Video S2 (play at 16-speed). Furthermore, the high-resolution TEM (HR-TEM) images indicated that there is no significant change of GSH-AuNCs before and after internalization into *A. acetii*, as shown in Figure S3. Moreover, the interactions between GSH-AuNCs and Gram-positive *S. aureus* were also examined using in situ liquid cell TEM. After 60 min of observation by in situ TEM, there was no significant morphological change in *S. aureus* incubated with GSH-AuNCs as shown in Supporting Information Figure S4. The reason can be attributed to the fact that GSH-AuNCs with amine groups on their surfaces

produced a much smaller amount of ROS in Gram-positive *S. aureus*.^{39,62} Overall, the results of real-time observations of *A. aceti* incubated with GSH-AuNCs indicated that interactions, including attachment, internalization, and destruction, between NCs and bacteria were observed by in situ liquid cell TEM.

Mechanism of the Death of *A. aceti* Induced by GSH-AuNCs. The detailed mechanism of GSH-AuNC-induced death of *A. aceti* is illustrated in Figure 5. Based on the results of real-time observations by in situ liquid cell TEM, GSH-AuNCs first attached to the bacterial membrane of *A. aceti* by physical adsorption.⁶² After attachment, GSH-AuNCs interacted with the bacterial membrane of *A. aceti* and further penetrated into *A. aceti* by internalization. Once inside *A. aceti*, GSH-AuNCs induced the production of ROS which resulted in antibacterial activity. Previous studies have demonstrated that a TEM electron beam creates ROS within the bacteria and the ROS generation can be enhanced by gold nanoparticles in the liquid.^{64–66} Herein, the bacteria of *A. aceti* were incubated with GSH-AuNCs in TEM liquid cell for 100 min without TEM electron beam irradiation. After incubation for 100 min, the sample of *A. aceti* incubated with GSH-AuNCs was observed by in situ liquid cell TEM. As shown in the Supporting Information, Figure S5, *A. aceti* revealed obvious damage. The result indicated that the TEM electron beam induced no significant ROS generation. The bacterial membrane of *A. aceti* was gradually destroyed with an increase in ROS induced by GSH-AuNCs. Eventually, the bacteria were completely destroyed.

CONCLUSIONS

In conclusion, GSH-AuNCs were successfully synthesized via a simple hydrothermal method. The optical and structural properties of the GSH-AuNCs were confirmed by UV–vis spectroscopy, XPS, fluorescence spectroscopy, FTIR spectroscopy, SEM, and EDX. Results of bacterial growth curves demonstrated that the antibacterial activity of GSH-AuNCs against *A. aceti* increased with the weight concentration. The antibacterial activity of GSH-AuNCs was ascribed to intracellular ROS generation caused by the GSH-AuNCs based on the results of the H₂DCFDA assay. Real-time observations of interactions between the GSH-AuNCs and *A. aceti* were accomplished using in situ liquid cell TEM. According to the real-time observations by in situ liquid cell TEM, the antibacterial mechanism occurred by GSH-AuNCs first attaching onto the bacterial membrane of *A. aceti* by physical adsorption and then penetrating into *A. aceti* by internalization. In *A. aceti*, GSH-AuNCs induced the production of intracellular ROS which caused the destruction of the bacterial membranes of *A. aceti*. After the destruction of the bacterial membranes, *A. aceti* burst and eventually died.

ASSOCIATED CONTENT

Supporting Information

The Supporting Information is available free of charge at <https://pubs.acs.org/doi/10.1021/acssuschemeng.1c06714>.

Spectra of ROS levels of *A. aceti* incubated with GSH solution and the control experiment; in situ TEM images of *A. aceti* without glutathione-conjugated gold nanoclusters; HR-TEM images of GSH-AuNCs before and after internalization into *A. aceti*; in situ TEM images of *S. aureus* incubated with GSH-AuNCs; and in situ TEM image of *A. aceti* with GSH-AuNCs (PDF)

Real-time TEM video of *A. aceti* (MP4)

Real-time TEM video for GSH-AuNCs incubated with *A. aceti* (MP4)

AUTHOR INFORMATION

Corresponding Author

Tsung-Rong Kuo – Graduate Institute of Nanomedicine and Medical Engineering, College of Biomedical Engineering, Taipei Medical University, Taipei 11031, Taiwan; International PhD Program in Biomedical Engineering, College of Biomedical Engineering, Taipei Medical University, Taipei 11031, Taiwan; orcid.org/0000-0003-4937-951X; Email: trkuo@tmu.edu.tw

Authors

Jui-Chi Kuo – Graduate Institute of Nanomedicine and Medical Engineering, College of Biomedical Engineering, Taipei Medical University, Taipei 11031, Taiwan

Shih-Hua Tan – Graduate Institute of Nanomedicine and Medical Engineering, College of Biomedical Engineering, Taipei Medical University, Taipei 11031, Taiwan

Yu-Cheng Hsiao – International PhD Program in Biomedical Engineering, College of Biomedical Engineering and Graduate Institute of Biomedical Optomechatronics, College of Biomedical Engineering, Taipei Medical University, Taipei 11031, Taiwan; Stanford Byers Center for Biodesign, Stanford, California 94305-5428, United States; Cell Physiology and Molecular Image Research Center, Wan Fang Hospital, Taipei Medical University, Taipei 11696, Taiwan

Chinmaya Mutalik – International PhD Program in Biomedical Engineering, College of Biomedical Engineering, Taipei Medical University, Taipei 11031, Taiwan

Hui-Min Chen – Department of Anatomy and Cell Biology, School of Medicine, College of Medicine, Taipei Medical University, Taipei 11031, Taiwan

Sibidou Yougbaré – Institut de Recherche en Sciences de la Santé (IRSS-DRCO)/Nanoro, 03 BP 7192 Ouagadougou 03, Burkina Faso

Complete contact information is available at:

<https://pubs.acs.org/10.1021/acssuschemeng.1c06714>

Author Contributions

○J.-C.K., S.-H.T., and Y.-C.H. contributed equally to this work.

Notes

The authors declare no competing financial interest.

ACKNOWLEDGMENTS

The authors wish to acknowledge Materials Analysis Technology (MA-Tek) for their help in providing K-kits for this study. We also acknowledge the Ministry of Science and Technology, Taiwan (grant no.: MOST 109-2113-M-038-005-MY2) and the Taipei Medical University for financially supporting this work. We also would like to thank Dr. Chi-Ming Lee and Chun-Chih Liu for their help with materials characterizations at the TMU Core Facility Center.

REFERENCES

- (1) Du, Y. X.; Sheng, H. T.; Astruc, D.; et al. Atomically precise noble metal nanoclusters as efficient catalysts: A bridge between structure and properties. *Chem. Rev.* **2020**, *120*, 526–622.
- (2) Kang, X.; Zhu, M. Z. Tailoring the photoluminescence of atomically precise nanoclusters. *Chem. Soc. Rev.* **2019**, *48*, 2422–2457.

- (3) Zhou, M.; Higaki, T.; Hu, G. X.; et al. Three-orders-of-magnitude variation of carrier lifetimes with crystal phase of gold nanoclusters. *Science* **2019**, *364*, 279–282.
- (4) Wang, L. M.; Chen, W. L.; Zhang, D. D.; et al. Surface strategies for catalytic CO₂ reduction: From two-dimensional materials to nanoclusters to single atoms. *Chem. Soc. Rev.* **2019**, *48*, 5310–5349.
- (5) Chakraborty, I.; Pradeep, T. Atomically precise clusters of noble metals: Emerging link between atoms and nanoparticles. *Chem. Rev.* **2017**, *117*, 8208–8271.
- (6) Chen, T. K.; Lin, H. B.; Cao, Y. T.; et al. Interactions of metal nanoclusters with light: Fundamentals and applications. *Adv. Mater.* **2021**, No. 2103918.
- (7) Xiao, Y.; Wu, Z.; Yao, Q.; et al. Luminescent metal nanoclusters: Biosensing strategies and bioimaging applications. *Aggregate* **2021**, *2*, 114–132.
- (8) Yao, Q.; Yuan, X.; Chen, T.; et al. Engineering functional metal materials at the atomic level. *Adv. Mater.* **2018**, *30*, No. 1802751.
- (9) Narouz, M. R.; Osten, K. M.; Unsworth, P. J.; et al. N-heterocyclic carbene-functionalized magic-number gold nanoclusters. *Nat. Chem.* **2019**, *11*, 419–425.
- (10) Loynachan, C. N.; Soleimany, A. P.; Dudani, J. S.; et al. Renal clearable catalytic gold nanoclusters for in vivo disease monitoring. *Nat. Nanotechnol.* **2019**, *14*, 883–890.
- (11) Kwak, K.; Lee, D. Electrochemistry of atomically precise metal nanoclusters. *Acc. Chem. Res.* **2019**, *52*, 12–22.
- (12) Fahmi, M. Z.; Ou, K. L.; Chen, J. K.; et al. Development of bovine serum albumin-modified hybrid nanoclusters for magneto-fluorescence imaging and drug delivery. *RSC Adv.* **2014**, *4*, 32762–32772.
- (13) Weng, B.; Lu, K.-Q.; Tang, Z.; et al. Stabilizing ultrasmall Au clusters for enhanced photoredox catalysis. *Nat. Commun.* **2018**, *9*, No. 1543.
- (14) Miao, Y. B.; Chen, K. H.; Chen, C. T.; et al. A noninvasive gut-to-brain oral drug delivery system for treating brain tumors. *Adv. Mater.* **2021**, *33*, No. 2100701.
- (15) Liu, X. K.; Tseng, C. L.; Lin, L. Y.; et al. Template-free synthesis of mesoporous ce3nb07/ceo2 hollow nanospheres for label-free electrochemical immunosensing of leptin. *Sens. Actuators, B* **2021**, *341*, No. 130005.
- (16) Piatek, J.; Budnyak, T. M.; Monti, S.; et al. Toward sustainable li-ion battery recycling: Green metal-organic framework as a molecular sieve for the selective separation of cobalt and nickel. *Sens. Actuators, B* **2021**, *9*, 9770–9778.
- (17) Hong, J. Y.; Wang, Y. X.; Zhu, L. Y.; et al. An electrochemical sensor based on gold-nanocluster-modified graphene screen-printed electrodes for the detection of beta-lactoglobulin in milk. *Sensors* **2020**, *20*, No. 3956.
- (18) Kuo, T.-R.; Liao, H.-J.; Chen, Y.-T.; et al. Extended visible to near-infrared harvesting of earth-abundant FeS₂-TiO₂ heterostructures for highly active photocatalytic hydrogen evolution. *Green Chem.* **2018**, *20*, 1640–1647.
- (19) Yougbare, S.; Mutalik, C.; Okoro, G.; et al. Emerging trends in nanomaterials for antibacterial applications. *Int. J. Nanomed.* **2021**, *16*, 5831–5867.
- (20) Yougbare, S.; Chou, H. L.; Yang, C. H.; et al. Facet-dependent gold nanocrystals for effective photothermal killing of bacteria. *J. Hazard. Mater.* **2021**, *407*, No. 124617.
- (21) Mutalik, C.; Okoro, G.; Krisnawati, D. I.; et al. Copper sulfide with morphology-dependent photodynamic and photothermal antibacterial activities. *J. Colloid Interface Sci.* **2022**, *607*, 1825–1835.
- (22) Li, Y. J.; Wang, C.; Wang, W. Y.; et al. Enhanced chemical immobilization and catalytic conversion of polysulfide intermediates using metallic mo nanoclusters for high-performance li-S batteries. *ACS Nano* **2020**, *14*, 1148–1157.
- (23) Zhang, H.; Liu, H.; Tian, Z.; et al. Bacteria photosensitized by intracellular gold nanoclusters for solar fuel production. *Nat. Nanotechnol.* **2018**, *13*, 900–905.
- (24) Chang, T.-K.; Cheng, T.-M.; Chu, H.-L.; et al. Metabolic mechanism investigation of antibacterial active cysteine-conjugated gold nanoclusters in *Escherichia coli*. *ACS Sustainable Chem. Eng.* **2019**, *7*, 15479–15486.
- (25) Cheng, T. M.; Chu, H. L.; Lee, Y. C.; et al. Quantitative analysis of glucose metabolic cleavage in glucose transporters overexpressed cancer cells by target-specific fluorescent gold nanoclusters. *Anal. Chem.* **2018**, *90*, 3974–3980.
- (26) Chu, G. Y.; Zhang, C. L.; Liu, Y. F.; et al. A gold nanocluster constructed mixed-metal metal-organic network film for combating implant-associated infections. *ACS Nano* **2020**, *14*, 15633–15645.
- (27) Yougbare, S.; Chang, T.-K.; Tan, S.-H.; et al. Antimicrobial gold nanoclusters: Recent developments and future perspectives. *Int. J. Mol. Sci.* **2019**, *20*, No. 2924.
- (28) Mutalik, C.; Wang, D. Y.; Krisnawati, D. I.; et al. Light-activated heterostructured nanomaterials for antibacterial applications. *Nanomaterials* **2020**, *10*, No. 643.
- (29) Yougbare, S.; Mutalik, C.; Krisnawati, D. I.; et al. Nanomaterials for the photothermal killing of bacteria. *Nanomaterials* **2020**, *10*, No. 1123.
- (30) Wu, X. Q.; Xu, H.; Luo, F. Z.; et al. Sizes and ligands tuned gold nanocluster acting as a new type of monoamine oxidase b inhibitor. *Biosens. Bioelectron.* **2021**, *189*, No. 113377.
- (31) Zhang, B.; Chen, C. B.; Chuang, W.; et al. Size transformation of the Au₂₂(SG)₁₈ nanocluster and its surface-sensitive kinetics. *J. Am. Chem. Soc.* **2020**, *142*, 11514–11520.
- (32) Li, C.-H.; Kuo, T.-R.; Su, H.-J.; et al. Fluorescence-guided probes of aptamer-targeted gold nanoparticles with computed tomography imaging accesses for in vivo tumor resection. *Sci. Rep.* **2015**, *5*, No. 15675.
- (33) Kaur, N.; Aditya, R. N.; Singh, A.; et al. Biomedical applications for gold nanoclusters: Recent developments and future perspectives. *Nanoscale Res. Lett.* **2018**, *13*, No. 302.
- (34) Hsu, P.-H.; Yougbare, S.; Kuo, J.-C.; et al. One-pot synthesis of thiol-modified liquid crystals conjugated fluorescent gold nanoclusters. *Nanomaterials* **2020**, *10*, No. 1755.
- (35) Zhang, H.; Cao, Y. H.; Xu, D. W.; et al. Gold-nanocluster-mediated delivery of sirna to intact plant cells for efficient gene knockdown. *Nano Lett.* **2021**, *21*, 5859–5866.
- (36) Wen, Q.; Yi, S. L.; Lin, Q. L.; et al. Terminal protection of peptides by interactions with proteins: A “signal-on” peptide-templated gold nanocluster beacon for label-free protein detection. *Talanta* **2021**, *233*, No. 122566.
- (37) Li, Q. Z.; Pan, Y. T.; Chen, T. K.; et al. Design and mechanistic study of a novel gold nanocluster-based drug delivery system. *Nanoscale* **2018**, *10*, 10166–10172.
- (38) Xie, Y.; Liu, Y.; Yang, J.; et al. Gold nanoclusters for targeting methicillin-resistant *Staphylococcus aureus* in vivo. *Angew. Chem., Int. Ed.* **2018**, *57*, 3958–3962.
- (39) Wang, Y. X.; Malkmes, M. J.; Jiang, C.; et al. Antibacterial mechanism and transcriptome analysis of ultra-small gold nanoclusters as an alternative of harmful antibiotics against gram-negative bacteria. *J. Hazard. Mater.* **2021**, *416*, No. 126236.
- (40) Zheng, K.; Setyawati, M. I.; Leong, D. T.; et al. Antimicrobial gold nanoclusters. *ACS Nano* **2017**, *11*, 6904–6910.
- (41) Zhu, Y. P.; Kuo, T. R.; Li, Y. H.; et al. Emerging dynamic structure of electrocatalysts unveiled by in situ X-ray diffraction/absorption spectroscopy. *Energy Environ. Sci.* **2021**, *14*, 1928–1958.
- (42) Kuo, T. R.; Chen, W. T.; Liao, H. J.; et al. Improving hydrogen evolution activity of earth-abundant cobalt-doped iron pyrite catalysts by surface modification with phosphide. *Small* **2017**, *13*, No. 1603356.
- (43) Low, J. X.; Dai, B. Z.; Tong, T.; et al. In situ irradiated X-ray photoelectron spectroscopy investigation on a direct z-scheme TiO₂/CdS composite film photocatalyst. *Adv. Mater.* **2019**, *31*, No. 1802981.
- (44) Dong, J. C.; Zhang, X. G.; Briega-Martos, V.; et al. In situ raman spectroscopic evidence for oxygen reduction reaction intermediates at platinum single-crystal surfaces. *Nat. Energy* **2019**, *4*, 60–67.

- (45) Goudar, V. S.; Yeh, P. H.; Wu, S. Y.; et al. Live circulating tumour cells selection on digitized self-assembled cell array (digi-saca) chip by in-parallel/in-situ image analysis, cell capture, and cultivation. *Sens. Actuators, B* **2020**, *316*, No. 128002.
- (46) Tung, C. W.; Kuo, T. R.; Hsu, C. S.; et al. Light-induced activation of adaptive junction for efficient solar-driven oxygen evolution: In situ unraveling the interfacial metal-silicon junction. *Adv. Energy Mater.* **2019**, *9*, No. 1901308.
- (47) Zhu, Y. P.; Chen, H. C.; Hsu, C. S.; et al. Operando unraveling of the structural and chemical stability of p-substituted CoSe₂ electrocatalysts toward hydrogen and oxygen evolution reactions in alkaline electrolyte. *ACS Energy Lett.* **2019**, *4*, 987–994.
- (48) Lee, T. S.; Patil, S. B.; Kao, Y. T.; et al. Real-time observation of anion reaction in high performance all ion batteries. *ACS Appl. Mater. Interfaces* **2020**, *12*, 2572–2580.
- (49) Asoro, M. A.; Kovar, D.; Ferreira, P. J. In situ transmission electron microscopy observations of sublimation in silver nanoparticles. *ACS Nano* **2013**, *7*, 7844–7852.
- (50) Zhu, M.; Aikens, C. M.; Hollander, F. J.; et al. Correlating the crystal structure of a thiol-protected Au₂₅ cluster and optical properties. *J. Am. Chem. Soc.* **2008**, *130*, 5883–5885.
- (51) Shamsipur, M.; Molaabasi, F.; Sarparast, M.; et al. Photoluminescence mechanisms of dual-emission fluorescent silver nanoclusters fabricated by human hemoglobin template: From oxidation- and aggregation-induced emission enhancement to targeted drug delivery and cell imaging. *ACS Sustainable Chem. Eng.* **2018**, *6*, 11123–11137.
- (52) Shang, L.; Dong, S.; Nienhaus, G. U. Ultra-small fluorescent metal nanoclusters: Synthesis and biological applications. *Nano Today* **2011**, *6*, 401–418.
- (53) Luo, Z.; Yuan, X.; Yu, Y.; et al. From Aggregation-Induced Emission of Au(I)–Thiolate Complexes to Ultrabright Au(0)@Au(I)–Thiolate Core–Shell Nanoclusters. *J. Am. Chem. Soc.* **2012**, *134*, 16662–16670.
- (54) Goswami, N.; Yao, Q. F.; Luo, Z. T.; et al. Luminescent metal nanoclusters with aggregation-induced emission. *J. Phys. Chem. Lett.* **2016**, *7*, 962–975.
- (55) Yu, Y.; Luo, Z. T.; Chevrier, D. M.; et al. Identification of a Highly Luminescent Au-22(SG)(18) Nanocluster. *J. Am. Chem. Soc.* **2014**, *136*, 1246–1249.
- (56) Bera, D.; Goswami, N. Driving forces and routes for aggregation-induced emission-based highly luminescent metal nanocluster assembly. *J. Phys. Chem. Lett.* **2021**, *12*, 9033–9046.
- (57) Wu, Z.; Yao, Q.; Zang, S.-q.; et al. Aggregation-induced emission in luminescent metal nanoclusters. *Natl. Sci. Rev.* **2020**, *8*, No. nwa208.
- (58) Wu, Z. N.; Yao, Q. F.; Chai, O. J. H.; et al. Unraveling the impact of gold(i)-thiolate motifs on the aggregation-induced emission of gold nanoclusters. *Angew. Chem., Int. Ed.* **2020**, *59*, 9934–9939.
- (59) Huang, P.; Jiang, Q.; Yu, P.; et al. Alkaline post-treatment of cd(II)–glutathione coordination polymers: Toward green synthesis of water-soluble and cytocompatible CdS quantum dots with tunable optical properties. *ACS Appl. Mater. Interfaces* **2013**, *5*, 5239–5246.
- (60) Ma, X.; Guo, Q.; Xie, Y.; et al. Green chemistry for the preparation of l-cysteine functionalized silver nanoflowers. *Chem. Phys. Lett.* **2016**, *652*, 148–151.
- (61) Nieto-Ortega, B.; Bürgi, T. Vibrational properties of thiolate-protected gold nanoclusters. *Acc. Chem. Res.* **2018**, *51*, 2811–2819.
- (62) Zheng, K.; Setyawati, M. I.; Leong, D. T.; et al. Observing antimicrobial process with traceable gold nanoclusters. *Nano Res.* **2021**, *14*, 1026–1033.
- (63) Zheng, K.; Xie, J. Cluster materials as traceable antibacterial agents. *Acc. Mater. Res.* **2021**, *2*, 1104–1116.
- (64) Woehl, T. J.; Kashyap, S.; Firlar, E.; et al. Correlative electron and fluorescence microscopy of magnetotactic bacteria in liquid: Toward in vivo imaging. *Sci. Rep.* **2014**, *4*, No. 6854.
- (65) Gupta, T.; Schneider, N. M.; Park, J. H.; et al. Spatially dependent dose rate in liquid cell transmission electron microscopy. *Nanoscale* **2018**, *10*, 7702–7710.
- (66) Korpanty, J.; Parent, L. R.; Gianneschi, N. C. Enhancing and mitigating radiolytic damage to soft matter in aqueous phase liquid-cell transmission electron microscopy in the presence of gold nanoparticle sensitizers or isopropanol scavengers. *Nano Lett.* **2021**, *21*, 1141–1149.

**HAZARD AWARENESS
REDUCES LAB INCIDENTS**

**ACS Essentials of
Lab Safety for
General Chemistry**

A new course from the
American Chemical Society

ACS Institute
Learn. Develop. Excel.

EXPLORE
ORGANIZATIONAL
SALES
solutions.acs.org/essentialsoflabsafety

REGISTER FOR
INDIVIDUAL ACCESS
institute.acs.org/courses/essentials-lab-safety.html